Patterned Plasma Immersion Exposure of Insulating Materials for the Purpose of Modifying Optical Properties

A thesis submitted in partial fulfillment of the requirement for the degree of Bachelor of Science with Honors in Physics from the college of William and Mary in Virginia

By

Linton Wells III

Accepted for ______________________________

(Honors, High Honors, or Highest Honors)

____

Director

____

____

____

Williamsburg, Virginia

April 2000

Contents:

1) Introduction
- Description of Ion Implantation
- Basic idea of Plasma Immersion Ion Implantation (PIII)

2) Previous Work
- Implanting Conductors
- Implanting Insulators

3) Theory
- Sheath Effects
- Implantation Depth and Density
- RC circuits and the internal resistance of thin films

4) Experimental Setup
- Apparatus
- Experimental target
- Aluminum coating
- Slide holder
- Mask
- Experimental specificationsÑomputer modeling
- Experimental Procedure

5) Data/Results
- Macroscopic Features
- Optical Microscopy
- Ellipsometry
- AFM
- SEM

6) Summary
- Conclusions
- Applications
- Future Work

7) Acknowledgements

Works Cited

Abstract:

Plasma immersion ion implantation was performed with an insulator as the work piece. Carbon dioxide was implanted into soda-lime glass, with pulse voltages of 25kV, and an implanted dose of $6x10^{16}$ ions/cm^2. Charge build-up due to the incident ion current leading to arcing across the surface of the glass was prevented by means of a 10 nm layer of aluminum over the surface of the implanted glass. Due to operating conditions of low plasma power and low chamber pressure, an unintended layer of SiO_2 was deposited on the surface. Optical as well as morphological changes in the glass were identified using optical microscopy, ellipsometry, AFM, and SEM. Using masks, circular areas as small as 50 μm in diameter were defined and successfully modified. Optical changes include a dramatic drop in the index of refraction of light at incident wavelengths greater than 600 nm.

Chapter 1

Introduction

1.1 Description of Ion Implantation

Ion implantation is an important surface modification process in which ions are buried just below the surface of a target object. It was originally developed as a means of doping semiconductors for use in integrated circuits. Since then, it has been shown that ion implantation of industrial metals and alloys can improve many of their surface properties. Some examples where implantation has proven beneficial are in improving friction characteristics, increasing corrosion and wear resistance, and making a surface harder.

Ion implantation can be contrasted against more conventional surface modification and coating technologies in that it does not add a layer of material on top of the treated object. Because implantation instead imbeds a graded distribution of material into the object, the material has a much greater adhesion to the object; it is less likely to delaminate. In addition, implantation does not require high processing temperatures, which could damage some more sensitive objects.

1.2 Plasma Immersion Ion Implantation

In Plasma Immersion Implantation (PIII), as distinguished from Beam Ion Implantation, the object to be implanted (work piece) is surrounded by a plasma. A large negative electrical pulse is applied to the work piece to accelerate positive ions from the plasma into just below the surface of the work piece. The energy per ion ranges from 10 to

100 keV, over which range of energies the average depth of implantation is typically a few tenths of a micron beneath the surface. Theoretically, these positive ions will strike all parts of the target at a normal incidence (perpendicular to the surface), which is the optimal angle for accurately controlling the implantation.

There are several advantages to using the plasma immersion technique. Irregularly shaped objects can be implanted with ease because they are immersed in the plasma, so the ions are pulled in uniformly over the surface. Uniformity can be ensured by surrounding the sample with a uniform plasma. In addition, whole work piece is implanted at once. As a result, large objects can be reliably done in a reasonably short time; a thin beam of ions does not need to trace back and forth across the surface. Similarly, no manipulation of the object is necessary during the implantation; for example, the work piece does not need to be turned around in order to focus the beam on the backside. Finally, the plasma immersion technique tends to be more efficient because it has high "throw," that is, very little of the energy is dissipated elsewhere. All of the ion’s energy is directed radially towards the work piece to be implanted.

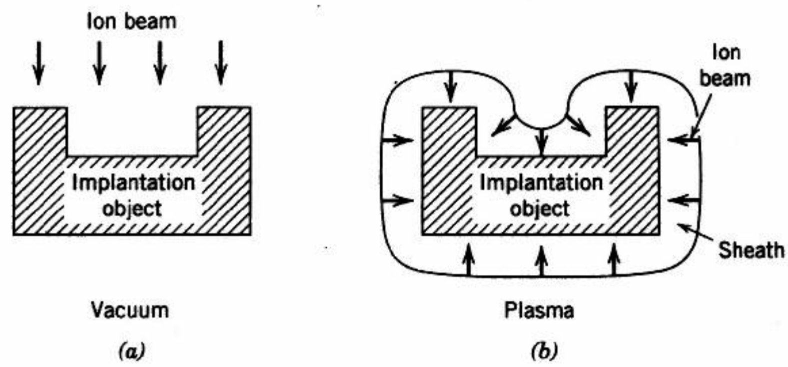

Figure 1.1 Different types of ion implantation. a) Work piece in a vacuum chamber under beam ion implantation. b) Work piece being implanted by PIII. [1]

Chapter 2

Previous Work

2.1 Implanting Conductors

Beam ion implantation was first developed for the doping of semiconducting materials. Similarly, PIII has also proved useful in semiconductor doping. As mentioned above, it offers many advantages over the traditional beam method because of its high dose rate, low energies, large implant areas, and lack of charging problems [2, 3]. In addition, because the implantation can be done at relatively low temperatures, it has the advantage of reducing diffusion after implantation, as well as expending a minimum of the thermal budget of the processed piece.

In addition to semiconductor doping, ion implantation has been shown to improve the surface properties of other materials. Improvements tend to be particularly effective because they are imbedded into the surface, and so do not wear or delaminate easily. Although nitrogen is most commonly implanted, a wide range of species has been implanted into an even wider range of target materials in order to examine how surface properties change. Nitrogen is so common because it is easy to make stable nitrides that improve many desirable material surface characteristics. For example, nitrogen implantation has been shown [5, 6] to improve the usable lifetime of orthopedic alloys and Co/WC drill bits by at least a factor of two. Analysis suggests that the performance improvement is due primarily to nitride formation at or near the surface [5].

PIII is more effective than standard beam ion implantation in improving surface characteristics of materials because, in theory, the whole work piece may be uniformly implanted at once, eliminating the need for line of sight access to the target. Many experiments with PIII systems have been conducted to confirm or improve these assertions about the geometry of implantation. High frequency, low-voltage pulse modulators have been developed to enhance implant uniformity and to increase the thickness of the modified layer [7]. Non-standard target geometries are also being tried, to confirm that irregular shapes or the insides of cavities can be implanted uniformly [8, 9, 10]. Other experiments [11] have increased implantation depth by combining a high pulse rate, voltage and current density to cause heating of the work piece, resulting in increased thermal diffusion of the implanted ions. This effort has yielded implanted nitrogen diffusion to depths greater than 1 μm.

A final method of surface modification has been developed with PIII, though it does not necessarily involve complete implantation, as such. Diamond-like carbon (DLC) films are chemically inert and extremely hard, with a very low coefficient of friction. They have great promise as protective coatings against scratching and abrasion [12]. To deposit a film on the target, very low pulse voltages are used to deposit carbon ions on the surface of the target that than to implant them. As the pulse voltage increases, however, the mode of surface modification goes from deposition to a mixture of deposition and implantation to pure implantation, each of which has differing effects on the surface of the material.

2.2 Implanting Insulators

Until now, PIII experiments have involved metallic or semi-conductor targets because these materials are best suited to carry the biasing pulse. An exciting next step has been taken by the William and Mary Group to implant insulting materials, such as glass. However, in preliminary work they found that the glass surface tended to charge and to arc prohibitively. In this thesis, I have proposed to coat the glass with an extremely thin layer (about 10 nm) of a conductor, such as aluminum, intended to serve as a conductive path to bleed the charge away between implant pulses. This layer would ensure the insulator surface that is exposed to the plasma returns to the neutral initial condition after every pulse, rather than remaining charged and producing the damaging electrical arcs encountered previous attempts.

Since there will be an extra layer between the plasma and the surface of the target, there will be a reduction in the depth of implantation achievable into the target material. This effect can be made slight if the conductive layer is kept thin enough so as to allow incident ions to pass through with enough energy to implant into the surface of the material. In addition, the conductive layer will be sputtered away by the incident ions over the course of the implantation, reducing even further the detrimental effect it has on implantation depth. Care must be taken to ensure that it remains thick enough to provide ample conductive paths to ground, in order to carry away any accumulating charge.

Chapter 3

Theory

3.1 Implantation Process

As mentioned above, in PIII processing, the workpiece is submerged in a plasma of the species to be implanted. Typically the plasma is weakly ionized (less than 5%) [18]. The implantation process starts with a high voltage pulse of the workpiece (typically 15-100 kV), which causes it to be negatively biased. This sudden negative biasing produces a negative electric field, which has two effects. First, electrons in the immediate vicinity of the target are accelerated away by the sudden introduction of the negative field. Next, as electrons leave the area, revealed positive ions begin to feel the effects of the field and are accelerated towards the workpiece.

As the incident ions impact the workpiece, their positive charge begins to cancel the negatively charged pulse. In between voltage pulses, since the charge on the target has been neutralized by incident ions, the plasma restores due to thermal motion and gas flow. The process is repeated with every pulse.

3.2 Sheath Effects

The electron repulsion and ion acceleration mentioned in the first part of this chapter can be thought of as a two-step process. The electrons respond in a time on the order of the inverse electron plasma frequency (ω_e^{-1}, ~1 μs, typically), which is far less than the inverse

ion frequency (ω_i^{-1}, ~1 ms) and so have usually left the area well before the ions begin accelerating. The ions are exposed rapidly compared to their ability to move, so when they first begin accelerating, they can be thought of as distributed uniformly through the plasma. This uniform distribution is known as the ion matrix sheath [13]. The initial sheath thickness increases with negative pulse voltage V, and decreases with increased plasma density n, where V and n are related by:

$$S_o = \sqrt{\frac{2\varepsilon_0 V}{q_i n}} \qquad (3.1)$$

where q_i is the charge on the ion ($1.6\text{x}10^{-19}$ C), and ε_0 is the permetivity of free space ($8.85\text{x}10^{-12}$ C^2/Nm^2). Typically V is on the order 10 kV, while n is of 10^9 ions/cm^3.

Equation 3.1 only applies to the initial ion matrix sheath, during a time at the beginning of each pulse that is longer than the electron response time, but shorter than the ion response time [13]. As more ions implant, ions in the region around the object are depleted, the electrons are no longer shielded from the negative electric field, and so recede further from the work piece, deeper into the plasma, exposing more ions at the far edge of the sheath. As the sheath around the target grows, the capacitively charged workpiece voltage is reduced by the accumulating charge of the incident ions [14].

3.3 Implantation Depth and Density

The two main factors in implantation are the total number of ions implanted (fluence) and the depth of implantation (profile). One advantage of PIII is that these two factors can be controlled independently. The depth of implantation, or profile, is dependent on the

species implanted, the structure of the target material, and the energy of the incident ions, which itself is dependent on the voltage of the pulses. The greater the magnitude of the pulse, the more energy ions have when they strike the work piece, and the further they implant [14]. As mentioned above, the depth of implantation is a graded distribution in the surface, and is typically modeled by computer programs such as Profile Code or TRIM [15]. An example of a calculation done with Profile Code can be seen in section 4.7.

The fluence, or the number of ions implanted per area, ϕ (atoms/cm^2), depends on of the pulse width, ω (s), the pulse repetition rate, f (s^{-1}), the average atoms per ion, n, the ion current, I_i (A), the total run time, t (s), and the surface area of target, A (cm^2). These are related by:

$$\phi = \frac{\omega f n I_i t}{qA} \qquad (3.2)$$

Where q in this case is the charge on the proton (1.6 x 10^{-19} C). ω, f and t are determined by the settings on the apparatus used. Typically, ω in on the order of 10 μs, f is of the order 100 Hz, and t is of the order 10^4 s. The area, A, must be measured from the geometry of the work piece, while n and I_i must be calculated for each species and target used. The average atoms per ion, n, depends on the ion ratios in the plasma being used.

The other variable in the delivered dose equation that is a direct experimental parameter is I_i, the ion current, or the number of ions going into the target at any one time. There is difficulty determining this. What can be measured, using a current monitor at the secondary transformers, is the total current, I_t. I_t consists of the ion current, I_i, which is the

parameter of interest, the emitted electron current, I_e, which is the number of electrons leaving the work piece, and the displacement current, I_d, which is due to charging effects, sheath capacitance and circuit loading effects [14]. I_d has been measured by pulsing the workpiece without a plasma in the chamber. Thus, the currents relate as:

$$I_t = I_i + I_e + I_d \tag{3.3}$$

The net current into the workpiece, I_n, is then:

$$I_n = I_t - I_d = I_i + I_e = I_i(1+\gamma) \tag{3.4}$$

γ is the secondary electron emission coefficient, the average number of electrons emitted from the workpiece per incident ion. γ has been shown [16] to be approximately linearly dependent on ion velocity, so γ for any given voltage can be extrapolated:

$$\gamma_{Vp} = \gamma_{20}\sqrt{\frac{V_p}{20}} \tag{3.5}$$

where Vp is the pulse voltage in kV, γ_{Vp} is the secondary electron emission coefficient at that voltage, and γ is an experimentally determined value of γ for a pulse voltage of 20kV. In the case of oxygen incident on aluminum, γ_{20}= 1.32.

From the Equation 3.3, the ion current I_i, needed for the delivered dose calculation (Equation 3.2) can be expressed as:

$$I_i = \frac{I_t - I_d}{1+\gamma} \tag{3.6}$$

Substituting this into Equation 3.2 results in:

$$\phi = \frac{\omega f n t (I_t - I_d)}{q A (1 + \gamma)} \qquad (3.7)$$

When designing an experiment, the time of implantation necessary to obtain a particular dose is often desired. For that purpose, Equation 3.7 can be expressed as:

$$t = \frac{\phi q A (1 + \gamma)}{\omega f n (I_t - I_d)} \qquad (3.8)$$

3.4 RC circuit and Internal resistance of Thin Films

At this point the role of the conductive film on the surface of the implanted target need to be clarified. It does not carry a significant portion of the biasing pulse used to pull ions out of the plasma. This is essential, because the internal resistance of thin films tends to be many orders of magnitude greater than the resistance of the material in bulk. As a result, the internal resistance of the thin conductive layer will prevent any significant amount of current to be transmitted along it in the short time that any single biasing pulse will last. Therefore, we need to arrive at some way of understanding how ions can be pulled out of the plasma into the insulating material without employing the thin conductive layer to carry the biasing pulse.

As discussed in 3.2, the implantation pulse creates an ion matrix sheath around the work piece. As a result of the ion matrix sheath, a simplified model of the work piece can be thought of much as a capacitor. Thus, if the glass to be implanted is in good metallic contact with baseplate (see figure 4.1), then the glass can be thought of as a dielectric in a parallel plate capacitor. One plate of the ÒcapacitorÓ is the baseplate, the other plate is the edge of

the ion-matrix sheath in contact with the glass. The simple RC circuit diagram in figure 3.1 represents this.

In implantation, if the capacitor becomes fully charged, the charge on the side of the glass facing the ion-matrix sheath will equal the voltage on the baseplate. Thus the full implantation bias will be applied to the target.

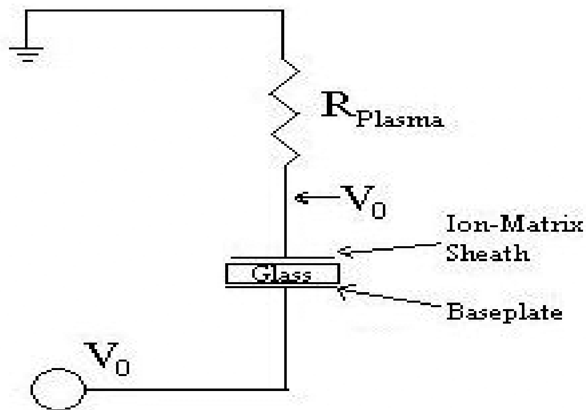

Figure 3.1: RC circuit diagram of the implantation, where the work piece is treated as a dielectric in a parallel plate capacitor.

It must be ensured that the length of the biasing pulse is long enough so that the ÒcapacitorÓ becomes fully charged.

The capacitance of a parallel plate capacitor with a dielectric depends on κ, the dielectric constant, A, the area of the two plates, and d, the separation between the plates. They relate by:

$$C = \frac{\kappa \varepsilon_0 A}{d} \tag{3.9}$$

Where, ε_0 is the permetivity of free space (8.85×10^{-12} $C^2/N\ m^2$).

The time constant, τ, of a RC circuit is:

$$\tau = R\ C \tag{3.10}$$

Where R=R_{plasma} in this case. τ is the amount of time it takes the capacitor to charge to 1/e of its total

The final charge on the capacitor is:

$$Q_f = VC \tag{3.11}$$

The charge on the capacitor as a function of time can be expressed as:

$$Q(t) = Q_f\left(1 - e^{-t/\tau}\right) = CV\left(1 - e^{-t/RC}\right) \tag{3.12}$$

Thus, if the implantation pulse is long enough to charge the capacitor to a significant percentage of its final charge, then the potential on both sides of the capacitor will be approximately equal, meaning that implantation will proceed unimpeded.

This emphasizes the role of the conducting thin film in implantation. It is purely to neutralize the extra positive charge produced by the incident ion current, I_i, rather than carrying any significant amount of the implantation charge. If it did carry the implantation charge, by Ohm's law, any amount of internal resistance of the film would reduce the potential by 1/R_{film}, significantly impeding the effectiveness of the implantation.

Chapter 4

Experimental Design

4.1 Apparatus

The William and Mary Plasma Immersion Ion Implantation system at the Applied Research Center consists of a large cylindrical implantation chamber, a vacuum pump system, a planar coil inductively coupled RF plasma source, and a pulse-forming network. Many aspects of this system, shown in figure 4.1 [18], have been previously described [17, 18].

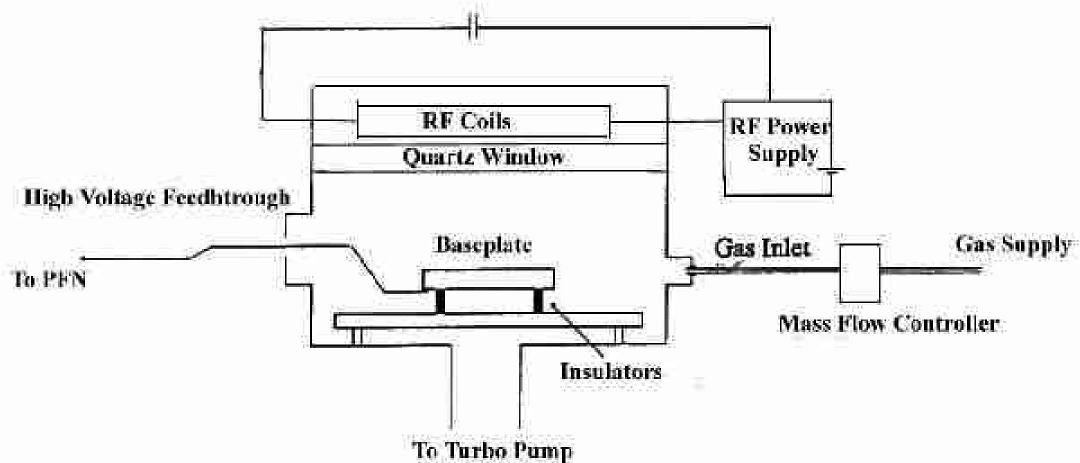

Figure 4. 1: A schematic of the William and Mary PIII implantation chamber

The chamber is cylindrical, 61 cm in diameter, by 51 cm high [18]. A 57 cm in diameter, 2.54 cm thick quartz window seals the top of the chamber. In addition to supporting the RF antenna coils, the window acts as the dielectric material for RF coupling to

ignite a plasma within the chamber [17]. Gas flows in through mass controllers. The plasma is ignited in the top portion of the chamber and allowed to drift down to the work piece, which rests on the base plate, in the middle of the chamber. This ensures the plasma uniformity needed to uniformly implant the surface of the work piece.

The planar coil inductively coupled RF plasma source provides 600 W of incident power, with 20-30 W reflected back by the plasma. Extremely late in this research program, we discovered that the condition of low power and low power density and low pressure was contributing to a significant amount of ÒcapacitiveÓ coupling capable of yielding significant sputtering of the quartz window. Under these conditions, SiO_2 (glass) is being continuously deposited on the sample at a low rate (0.001-0.05 nm/s) as the CO_2 implantation is occurring. We will have more to say about the consequences of this later.

The pulse-forming network (PFN) provides the biasing pulses to the work piece. Initially, it produces a maximum current of 300 A at 10 kV, which is sent through a 10:1 step up transformer, resulting in a peak voltage of 100 kV and 30 A. The high voltage pulse train cycles at 200 kHz. Pulses are square, 10 _s long, with < 1 _s rise and fall time, and < 10% ripple.

In the course of this research, system performance improvements have been made in both the pump system and the pulse-forming network. In the pump system, which consists of a turbo pump backed by a rough pump, the turbo pump was upgraded to a larger model. This improvement allows higher vacuums, on the order of 10^{-7} torr, to be attained in shorter time. Even though the operating pressure for implantation is only $8x10^{-4}$ torr, the ability to pump down to 10^{-7} torr is useful for cleaning work pieces in preparation for implantation.

Changes to the PFN have consisted of replacing the thyratron, the thyratron driver, the power supply and the reset circuit with more powerful versions, capable of creating stronger pulses. Even though they were not used in the current set of experiments, these improvements allow 100 kV pulses at 200 Hz to be obtained, rather than the previous limit of 50 kV pulses at approximately 100 Hz. In order to support these improvements, the PFN was also rewired from single phase to 3-phase power, with the appropriate interlocks and safeties added.

4.2 Experimental Target

To obtain the insulating material used as targets in the experiment, 7.62 cm x 2.54 cm (3Óx1Ó) glass laboratory slides, each sputter coated with a uniform 10 nm layer of aluminum were purchased from a vendor. The glass slide was made of common soda-lime glass.

4.3 Aluminum Coating

The conductive layer put on top of the glass was chosen to be aluminum, as opposed to gold, silver or copper, for four reasons. First, it is easy and inexpensive to plate onto glass. Second, it can be removed using hydrochloric acid, to examine the unimplanted glass as easily as the implanted glass. Third, it has a low Z (atomic number), and so can easily be implanted through without impeding the energy of the incident ions. Finally, aluminum is a good electric conductor, which allows it to efficiently carry away the charge build up during implantation.

Using aluminum does present problems, however. Aluminum does not bond to glass well, and so the layer can be very easy to damage or rub away. Second, a non-conducting aluminum oxide layer naturally forms on top of all aluminum exposed to the oxygen in air. This oxide layer can range from 2 nm to 4 nm into the surface of the aluminum [19]. This reduces the conductivity of the aluminum coat, impeding its effectiveness in PIII.

Regardless of the degree of oxidation, 10 nm was chosen for the thickness of the aluminum coating because it was certain to be thin enough so as to not impede implantation. Initial modeling using Profile Code, discussed in section 4.7, show that even with low energies, the 10 nm layer could be implanted through without impeding implantation. It was not as certain from the initial modeling that thicker layers would be as easily penetrated. Now that the 10 nm layer has proved to not hinder implantation, 20 nm or 30 nm of aluminum may be attempted, allowing for even greater implantation densities and energies to be achieved.

4.5 Slide Holder

Only the top of the slide is coated with a conductive layer, not the sides or bottom. Thus, the slide cannot simply be placed like a conductive sample on the implantation base plate for two reasons. First, the conductive aluminum coat will not have a path to ground along which to bleed away the accumulating charge. Second, the uncoated bottom and sides of the glass slide will charge excessively, causing damaging arcs.

To solve this sample mounting problem, a slide holder was designed and built. It consisted of two halves, each 10 cm square, and approximately 2 cm thick, made of stainless

steel. The halves were secured together by 4 stainless steel bolts at each corner. The lower half had two depressions, 7.62 cm long by 2.54 cm wide, made to a uniform depth of .5 mm. The goal was to fit the edges of the slides as closely as possible, so as to minimize any charging that occurs on the edge by conducting it away, while still allowing the surface of the slide to protrude above the rest of the bottom half. The upper half had two 5.08 cm long by 1.9 cm wide holes cut into it, positioned in the center of the depressions in the lower half. The goal was that when the slides were in the holder, they would be held firmly in place by the upper half, while still exposing aluminum surface to the plasma for implantation.

In addition to carrying the current to the top of the slide, holding the slide in place, and preventing charging along the side edges, the slide holder performs one other useful function. The bolts can be tightened so as to apply a moderate amount of pressure to the top of the slide. This pressure breaks the aluminum oxidation layer that naturally forms on the aluminum, allowing for a conductive path to form.

4.6 Masking

When doing these PIII studies a mask partially covers the work-piece being implanted. This is done for a number of reasons. First, by causing a contrast between implanted and unimplanted areas on the same sample, the effects of the implantation can be discovered easily. Secondly, masking defines patterns on the surface, testing the level of detail that is possible in implantation.

Masks served two further purposes in this experiment. They carried the incident ion current from the surface of the aluminum to the slide holder. Secondly, by covering parts of

the surface, they reduce the distance that the aluminum coat has to carry the accumulating charge, thereby minimizing the time needed to reset the implanted region to neutral charge. Thus, even though the masks do not help the ions implant into the surface, they do help to neutralize the implanted region, allowing implantation to continue for multiple pulses.

The masks consisted of 200 µm thick stainless steel strips, 2 cm wide and approximately 10 cm long. Into the strips, whose pattern can be seen in figure 4.2, was burned a further pattern of holes using a copper vapor laser from Siemen's Company. The laser operated between 518-573 nm, had a power output of 20 W and a spot size 50 µm in diameter. Holes of varying diameter were made using a programmable trepanning head.

Four patterns were made. The first was a single 75 µm hole made at a 45¡ angle from the normal to the surface. It was made in preparation for future experiments that would simulate implantation of the sidewall of a vertical well. The next three patterns were made to test the detail that could be implanted. Each pattern is a set of four holes made perpendicular to the surface of the mask. The first set is of four 50 µm holes, separated by 100 µm. The next is a set of four 100 µm holes separated by 200 µm. This was done to see if the 50 µm set was too fine to be implanted through. The final set of four holes varies in size, one 50 µm, one 100 µm, one 200 µm and one 300 µm. These holes were each separated by 300 µm.

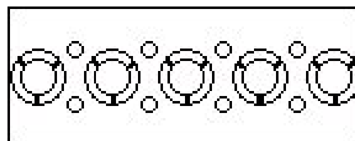

Figure 4. 2: Example of the mask, actual size. The patterned holes drilled are in the center of the large circles, but are too small to see at this macroscopic scale.

The masks were mounted within the slide holder to allow a large area to be implanted, to facilitate analysis by the ellipsometer later on (section 5.3).

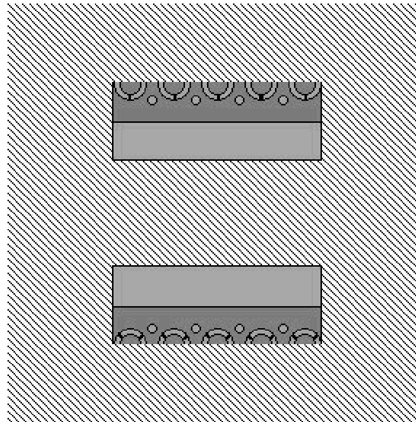

Figure 4. 3: Top-view of the slide holder, the mask, and the slide. The holder is crosshatched, the mask is dark gray, and the slide is light gray. The light gray area will be implanted.

4.7 Experiment Specifications--Computer modeling

An ion implantation modeling program, Profile Code, was used to determine the maximum fluency attainable before the aluminum coat was sputtered away due to ion impact. Implantations of carbon, oxygen and nitrogen were modeled, at energies of 10, 20, 25, 30, 50 and 100 keV, at a variety of different fluencies. It was determined that for carbon dioxide, a implantation fluency of approximately $2x10^{16}$ ions/cm^2 was the maximum that the aluminum coating could support and retain some degree of conductivity.

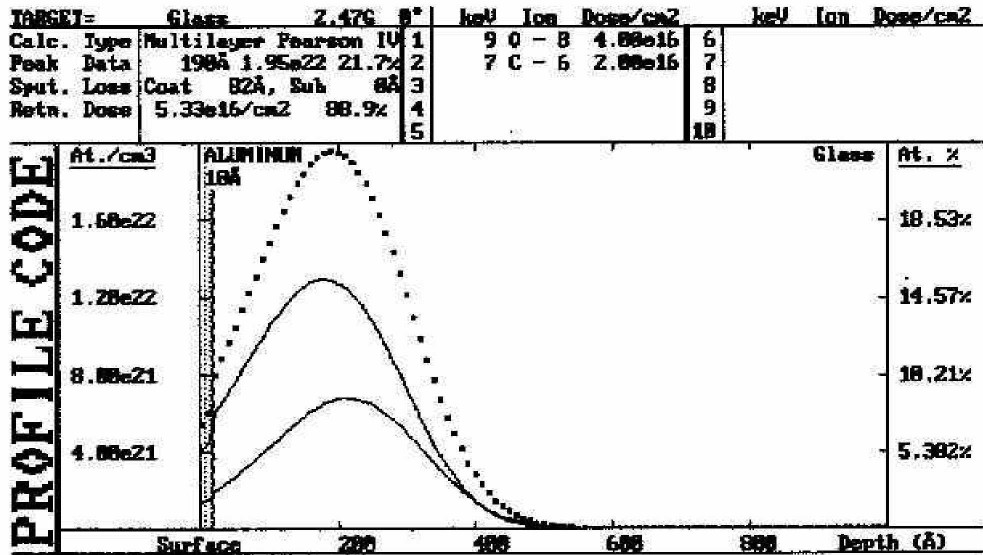

Figure 4. 4: Example of a Profile Code implantation depth profile of carbon dioxide implanted at an energy of 25 kV and a fluency of $2x10^{16}$ ions/cm^2. The implantation was modeled as if the carbon and two oxygens of the CO_2 molecule dissociated upon impact with the surface of the glass. This is reasonable, considering the energy of the implant (25 keV total per ion) is much greater than the binding energy of the molecule (4 eV). This model was run for both oxygen at $4x10^{16}$ ions/cm^2 and carbon at $2x10^{16}$ ions/cm^2, resulting in a total delivered fluency of $6x10^{16}$ ions/cm^2. The carbon is the lowest of the graphs, the oxygen is the middle, and the dotted line is the sum of the two. Note the 18 layer of aluminum that remains after the implant.

4.8 Experimental Procedure

Experiments consist of preparing the workpiece, setting the piece in the chamber, sealing the chamber, pumping down, plasma ignition, pulsing, plasma extinguishing, venting the system.

The work pieces, glass slides held in a slide holder and mask and coated with 10 nm of aluminum in this case, are prepared by standard cleaning procedures to eliminate contamination from oils and accumulated dust. All surfaces except for the aluminum top of the slide are wiped with 2-propanol and allowed to air-dry.

Pump down of the entire chamber usually takes from 30 to 45 min. This consists of an initial pumping to 10^{-3} torr by the rough pump of the whole chamber. Then the turbo pump is started, and is allowed to take the entire chamber down to at least 10^{-7} torr. Even though the implantation pressure is only $8x10^{-4}$ torr, the system is pumped to 10^{-7} torr because it serves to further clean the work piece and the inside of the chamber. A cleaner workpiece and chamber is less likely to arc.

Once the chamber has been pumped down, the working gas is introduced. A needle valve is used to balance the inflow of the gas with the outflow due to the pump, to arrive at a chamber pressure of $8x10^{-4}$ torr. Once this is achieved, the plasma can be ignited.

Radio frequency current is supplied by the power supply to the coil antenna resting on the quartz window above the chamber. The coils produce an electric field that is transmitted through the window into the chamber below. The species gas is ionized and a plasma results. The incident power used is approximately 600 W, with about 30 W reflected back to the source. There is no set value used for the incident power. As high a value as possible is set for the incident power, while keeping the reflected power below 30 W. Once the plasma has stabilized, a process that requires waiting a few minutes to ensure that the reflected power is stable, implantation can begin.

In the past, the glass charging has caused excessive arcing. The aluminum coat reduces, but does not completely eliminate the problem. Thus, when pulsing, rather than preset a desired implantation voltage, the voltage is slowly raised until an arc appears. The voltage is then dropped a few kV and implantation proceeds at that level. In each run, the arcing appeared at 27 kV, meaning the implantation was conducted at 25 kV.

As discussed in section 3.4, to ensure that the ion-matrix sheath on the surface of the glass feels the total potential applied to the work piece, the pulse length must be two or three times longer than the RC time constant, τ. To determine this, we use equation 3.9 to find the capacitance of the glass,

$$C = \frac{\kappa \varepsilon_0 A}{d}$$

where the dielectric constant of glass, $\kappa_{glass} = 5.4$. The thickness of the glass, d=1 mm. The surface area of the glass, A = (2.54cm) x (7.62cm) = 19.35 cm^2 = .001935 m^2. Thus, the capacitance is:

$$C = \frac{(5.4)(8.85 \times 10^{-12})(1.935 \times 10^{-3})}{(1 \times 10^{-3})} = 9.25x10^{-11}\,F$$

Plugging this into equation 3.10 give the time constant, τ:

$$\tau = RC$$

Where R is the resistance of plasma, R_{plasma}, and is the total resistance presented by the rest of the implantation plasma. It was measured by Venhaus [18] to be 100 Ω. Thus:

$$\tau = (100)(9.25 \times 10^{-11}) = 9.25 \times 10^{-9}\,s$$

Since the time constant of the capacitor is so much smaller than the pulse length of 1.5x10^{-5} s, we can be confident that the potential at the edge of the ion-matrix sheath is unimpeded by the glass, and is in fact, effectively the full 25 kV applied to the system.

Before the slide holder, masks and slides are placed in side the chamber, resistances between various points on the surface of the mask and the surface of the slide to the base of the slide holder are compared. This is done to check that the internal resistance of the

aluminum coat is not so great as to prevent charge from bleeding away during the time when the slide holder is not being pulsed by the implantation current. At the point furthest from the edge of the mask, where the mean free conductive path is greatest, the aluminum was found to have a resistance of approximately 10 Ω. This is compared to less than 0.1 Ω for the mask to the base of the slide holder. In order to compensate for this resistance discrepancy of approximately 100:1, the pulse rate is set to a relatively low value of 60 Hz. While this is far below the upgraded capabilities of the pulse-forming network, it ensures that the accumulating charge on the surface of the glass has as much time as possible to dissipate, even though the relatively high internal resistance of the aluminum coat hinders it.

We now have enough information to determine the length of time that will be spent implanting. As suggested by figure 4.4, beyond an implanted dose of 6×10^{16} ions/cm^2, the coating becomes too thin to support a current, preventing any further implantation into the glass. Thus, 6×10^{16} ions/cm^2 was the target dose. The run duration needed to obtain this dose is calculated using equation 3.8:

$$t = \frac{\phi q A (1 + \gamma)}{\omega f n (I_t - I_d)}$$

For a 25 kV implantation, the secondary electron coefficient, $\gamma_{25} = 1.47$, (equation 3.6). The total surface area of the slide holder with slides is 250 cm^2. The pulse width, w = 15×10^{-6} s. The pulse repetition rate, f = 60 s^{-1}. The average number of atoms per ion for carbon dioxide is $n_{CO_2} = 3$. The displacement current I_d, was negligible. The total target current, I_t, was measured using the current monitor: $I_t = 0.3$ A. Thus the duration needed to achieve the desired dosage at 25 kV was calculated as:

$$t = \frac{(6x10^{16})(1.6x10^{-19})(250)(1.47)}{(15x10^{-6})(60)(3)(.3)} = 6600s \cup 2hrs$$

After the appropriate amount of time, the pulse train is stopped and the plasma is quenched. The sample and chamber is still quite hot from interacting with a plasma for such an extended period of time. Thus, rather than venting the chamber to atmospheric pressure, which could cause thermal shock damage to both the chamber and the sample, the chamber is vented with nitrogen to a pressure of 1 torr, and allowed to cool over night.

Chapter 5

Results

5.1 Macroscopic Features

Exposed samples were cut using a diamond scribe into five pieces, each containing one of the five circular areas of the masks. The samples were then examined using optical microscopy, ellipsometry, atomic force microscopy (AFM) and secondary electron microscopy (SEM). Shortly before the termination of this research effort a new instrument (DEK-TAK) capable of performing profilometry to a high vertical resolution over large areas was installed in our laboratory. It was through the use of this instrument that the 200 nm SiO_2 deposition was confirmed.

Macroscopically, the slides had some obvious features. The aluminum layer, which appears opaque on the unexposed slides, had been removed or modified, rendering it Òtransparent.Ó The exposure yielded a slight brown tint to the area, when light was shined directly through the back of the slide. As the slide was tilted from side-to-side, however, a blue tint overcame the brown.

To provide evidence that the modified surface was not a loosely aggregated carbonaceous layer deposited on the surface, attempts were made to damage (scratch) or remove the modified layer. If this could be done, then any modifications resulting from the exposure would have reflected such a ÒsootyÓ carbon deposition. Attempts at removing the layer included rubbing it with pencil eraser, scratching it with a razor blade, and washing it with both propanol, and soap and water. None of these resulted in obvious removal of the

modification to the glass, suggesting that there is not an deposited (loose) overlay and that the optical changes observed have resulted either from implantation for from co-deposition of an ÒimplantedÓlayer whose hardness and other mechanical properties were Òglass-like.Ó

5.2 Optical Microscopy

The implanted areas were specifically examined under the optical microscope to look for evidence of signs of arc damage and to look for resulting changes in the optical properties of the glass. No arc damage was detected on the implanted areas of any of the glass slides, even at magnifications up to 600x. This lack of arc damage on any of the samples, which usually appears as burned holes or feathery streaks across the surface of the glass, indicates that charging effects were not a problem. This is evidence that the layer of aluminum successfully bled away the excess charge resulting from incident ions.

The optical microscope also offers some insight into the change in the optical properties of the glass. The change of color, from the clear of standard soda-lime glass to light blue, is the most obvious effect of the implant (see figure 5.1) creating a thin film that produces the optical properties observed. These properties will be studied in greater detail in the ellipsometry section, 5.3. The fact that this color change was seen under the 50 µm masked hole suggests that the modified features can be made by masking of at least down to diameters of 50µm.

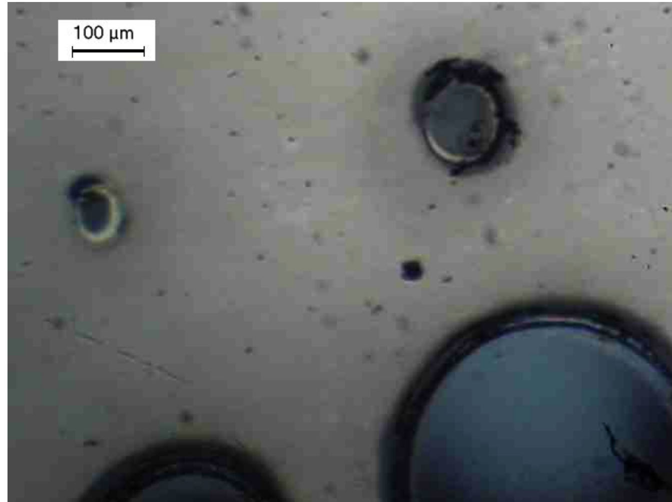

Figure 5. 1: The four circles are the implanted areas, which appear blue, examined under 60x magnification. The aluminum layer appears shiny gray. The largest of the implanted areas is 300µm in diameter, the smallest is 50µm in diameter, and the other two are 100 and 200µm, respectively. Note the evidence of surface modification in the 50µm hole. Note as well the blackened (damaged) areas around each of the circular implanted regions.

The darkened features at the edge of the circular exposed areas are likely due to a combination of several effects. First, if the stainless steel mask were to lift up off of the surface of the slide due to warping brought on by thermal expansion, then both the implantation plasma and the depositing SiO_2 would could have access to a greater area of slide surface. The simultaneous deposition of SiO_2 containing excess oxygen and carbon, combined with coating due to fast ion bombardment, leads to a large step-edge that may appear dark. This edge damage extending under the mask might also be increased by electric fields associated with the slide holder that have not been modeled. If the mask lifts sufficiently far off of the slide, there may be field lines that extend underneath the mask, guiding ions there, leading to more accumulation on the surface further underneath than might otherwise be

expected. The nature of this ÒtransitionÓ area at the edge of the exposed region will be further examined in section 5.4.

Another unexpected feature was the level of damage to the aluminum hidden under the mask, further than 500µm from the edge of an implanted area.

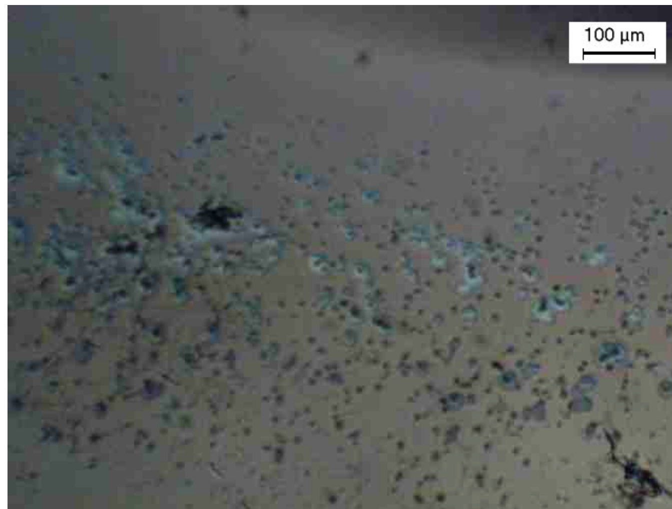

Figure 5. 2: An unimplanted region of glass, still covered by the 100 of aluminum, examined at 60x magnification. The damage appears as the swath of dark areas and craters in surface.

This damaged is most likely due to flaws in the aluminum, promoting an arc to the underside of the mask. Since the aluminum was held in such loose contact to the surface of the glass, arcs might create holes, causing the visible damage. It did not appear to have detrimental effects on the ability of the aluminum to carry away the charge, however.

5.3 Ellipsometry

Ellipsometry is a surface and thin film measurement technique that uses polarized light. A beam of light of known polarization is reflected off of the surface of the sample and

collected by a photodetector. The phase change as a result of interaction with the surface is measured and expressed in terms of Psi (Ψ) and Delta (Δ). These values relate to the Fresnel

$$\tan(\Psi)?e^{i\Delta} = \frac{r_p}{r_s}$$

reflection coefficients R_p and R_s for p- and s- polarized light, respectively.

Because ellipsometry measures the ratio of two values it can be highly accurate and very reproducible. Because the ratio is a complex number, it also has phase information (Δ), which makes the measurement very sensitive. Ellipsometry works best for film characterization when the film thickness is not much smaller or larger than the wavelength of light used for measurement. It is difficult to use a probe of wavelength 500 nm (or so) to characterize a 0.5 nm or a 10000 nm thick film, whereas films of 5 nm to 1000 nm are much simpler to characterize. As a result, ellipsometry is an ideal tool for characterizing the thin films that have been produced in this research.

Ellipsometry can determine the film thickness, index of refraction, n, coefficient of extinction, k, and many physical quantities of the film(s) that affect the optical constants. To determine these many different parameters, the ellipsometer does not measure the sample parameter of interest. Rather, it instead measures Ψ and Δ as a function of the parameters of interest. It is then necessary to solve the inverse problem of modeling the measured data to estimate values of the sample parameters which yield data predicted from the model which best matches the measured data. A computer run regression analysis is generally used to tackle this ÒfittingÓ problem. The Mean-squared Error (MSE) between the projected data and the experimental data determines the ÒgoodnessÓ of a modelÕs fit; a lower MSE reflects a

closer fit. The results of this data acquisition, modeling and fitting procedure will be presented here.

After examining the slides under the optical microscope, some of the samples were examined by the ellipsometer for two purposes. First, to quantify the optical changes apparent under the optical microscope. Second, to produce a depth profile to compare with the Profile Code simulations. Unfortunately, due to constraints of the spot size of the ellipsometer, none of the finely masked areas could be examined. Only the largest of the exposed areas could accommodate the spot, the same areas that had the most SiO_2 deposited. As a result of this, only three slides were examined using ellipsometry. One was an unexposed slide against which the other two would be compared. The other two were exposed slides, and will be referred to as A and B, for convenience.

All of the following spectra were taken a minimum of three times, at angles of 60°, 65°, 70° and 75°, on separate days with fresh calibrations to ensure consistency and accuracy of measurement. In all cases, for all slides, the results for Δ and ψ agreed to within 10%. All of the data presented here was reflected off of the sample at 75 degrees from the normal of the surface of the sample.

The first slide examined was the unmodified slide coated with 10 nm of aluminum. In constructing the model, in addition to the aluminum, we were certain that a 3-4 nm layer of aluminum oxide had formed over the surface due to its exposure to oxygen in the atmosphere [19]. Thus, the unmodified slide was modeled as:

2	al2o3	4.3369 nm
1	al	7.1358 nm
0	slide	1 mm

Figure 5. 3: Model of the unexposed slide coated with 10 nm of aluminum. The exact thickness of each layer was determined by a fit to the experimental data presented in figure 5.4. MSE to the data is 1.472

The data created from this model can be compared against the experimentally generated data in figure 5.4.

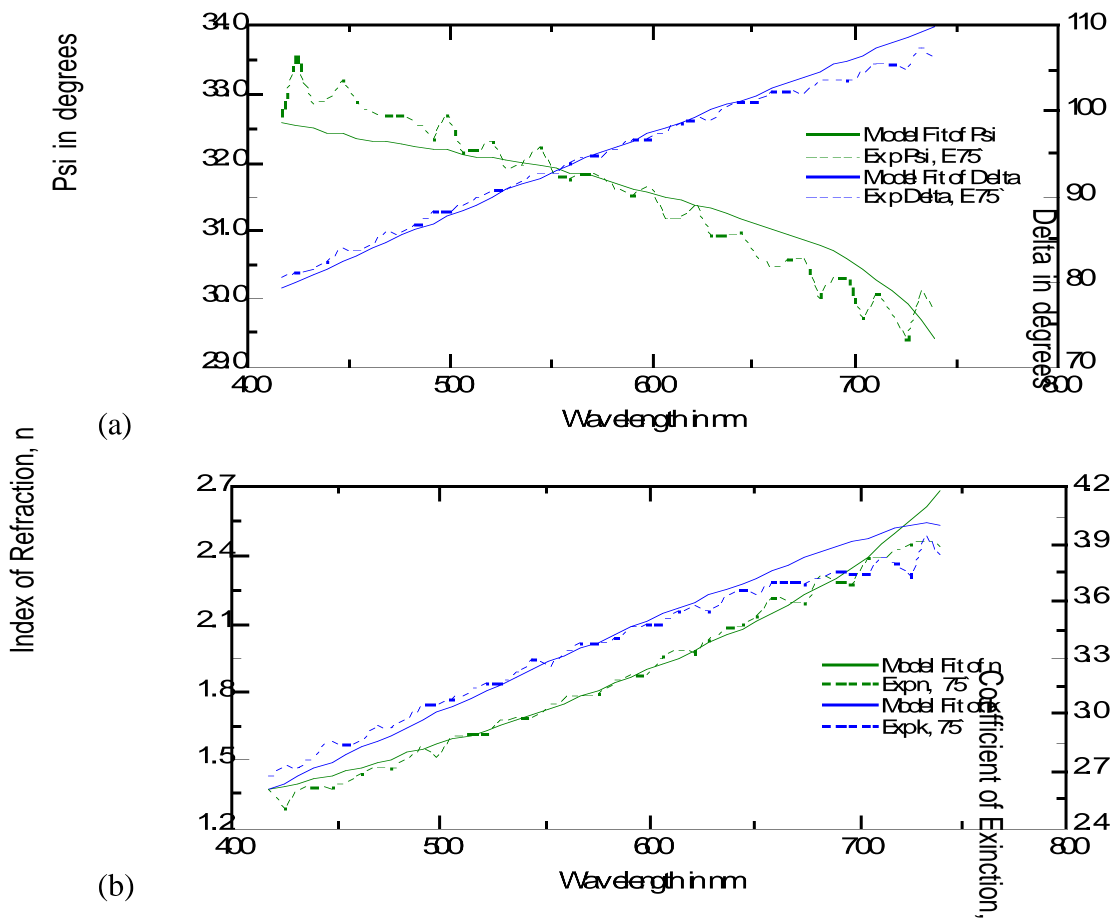

Figure 5. 4: Unexposed slide, experimental data and model fit data in terms of the wavelength of the incident polarized light. The model fit data derives from the model presented in figure 5.3. (a) Raw data directly from the ellipsometer, in terms of Psi and Delta. (b) Optical data, derived from the raw data using the Fresnel equations, in terms of the index of refraction, n, and the coefficient of extinction, k.

The most obvious optical feature of the unmodified slide is the rising curve of the coefficient of extinction, k, as a function of wavelength (figure 5.4). This is suggestive that the material being examined is opaque in the bulk, which agrees with macroscopically observed features of the unmodified slide, that it is opaque. While this is an unimpressive result, it does lend credence to the data aquired using the ellipsometer.

Now that the relatively easy task of analyzing a sample of known properies is complete, the more difficult application of ellipsometry to the unknown properties of the modified slide can begin. Both models of the modified slides A and B, were created with four layers. In the models, the base was composed of standard slide glass, 1mm thick, with known optical properties, which were not allowed to vary during the regression analysis. On top of it was placed a second layer of slide glass, whose thickness and optical properties were allowed to vary. This is to approximate implantation of carbon dioxide into the glass. The intial thickness of this layer was set at 30 nm to correspond with the Profile Code depth profile presented in figure 4.4. On top of the modified slide glass layer, a layer of SiO_2 was placed, whose thickness and optical constants were similarly allowed to vary during the regression analysis. This time it is to approximate carbon dioxide implantation to the accumulating layer of SiO_2. The initial thickness of the modified SiO_2 layer was set to 160 nm, and allowed to vary. The final layer on top was a layer of SiO_2 whose optical constants were not allowed to vary, but whose thickness was. This is due to the fact that the last few nanometers of SiO_2 will be implanted through, rather than in, and as such will remain

relatively pure. This Òcapping Ólayer was given an initial thickness of 40 nm, in order to arrive at a total SiO_2 deposition of 200 nm.

Now that the principles used to construct the two following models have been presented, the model arrived at for slide A is:

3	sio2	39.999 nm
2	implanted sio2 region	150.08 nm
1	implanted slide region	29.962 nm
0	slide	1 mm

Figure 5. 5: Model for modified Slide A. The exact thickness of each layer was determined by a fit to the experimental data presented in figure 5.6. MSE to the data is 0.742

Although all of the models presented are excellent fits to the experimental data, this is by far the model with the closest fit to the experimental data, with an MSE of 0.742.

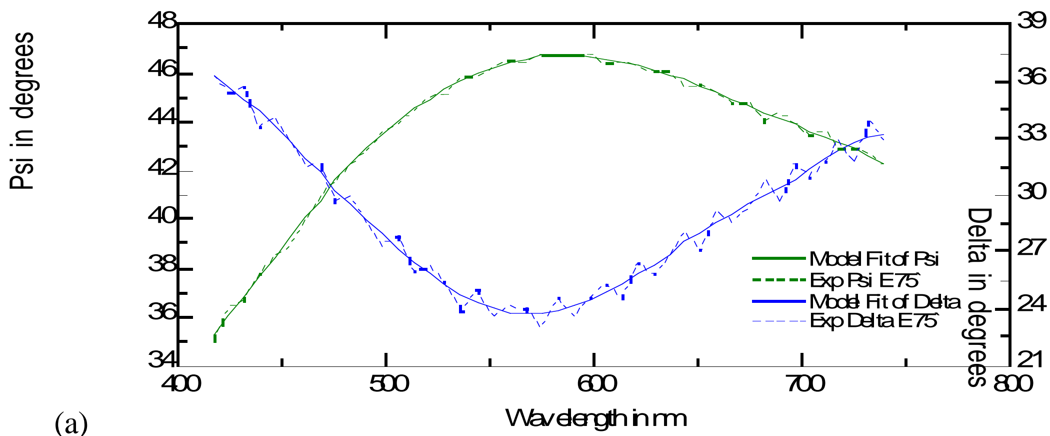

(a)

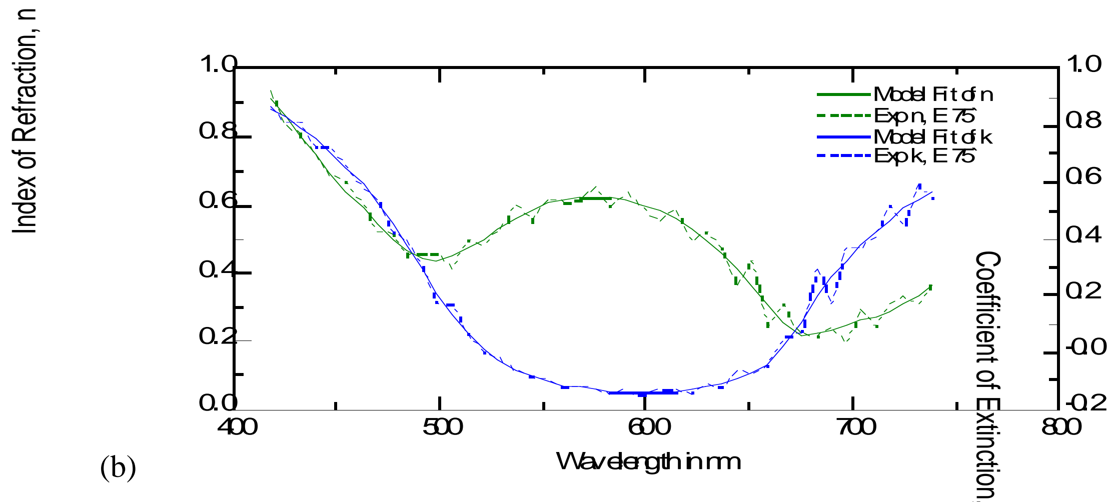

(b)

Figure 5. 6: Modified Slide A, experimental data and model fit data in terms of the wavelength of the incident polarized light. The model fit data derives from the model presented in figure 5.5. (a) Raw data directly from the ellipsometer, in terms of Psi and Delta. (b) Optical data, derived from the raw data using the Fresnel equations, in terms of the index of refraction, n, and the coefficient of extinction, k.

Using an initial model identical to the methods described for slide A, a model for slide B was constructed:

3	sio2	46.393 nm
2	implanted sio2 region	16986 nm
1	implanted slide region	31.752 nm
0	slide	1 mm

Figure 5. 7: Model for modified Slide B. **The exact thickness of each layer was determined by a fit to the experimental data presented in figure 5.8. MSE to the data is 2.119**

Note how in slide B the modified SiO_2 layer is significantly thicker than the similar layer in slide A. This suggests that slide B was more directly under the sputter source than slide A.

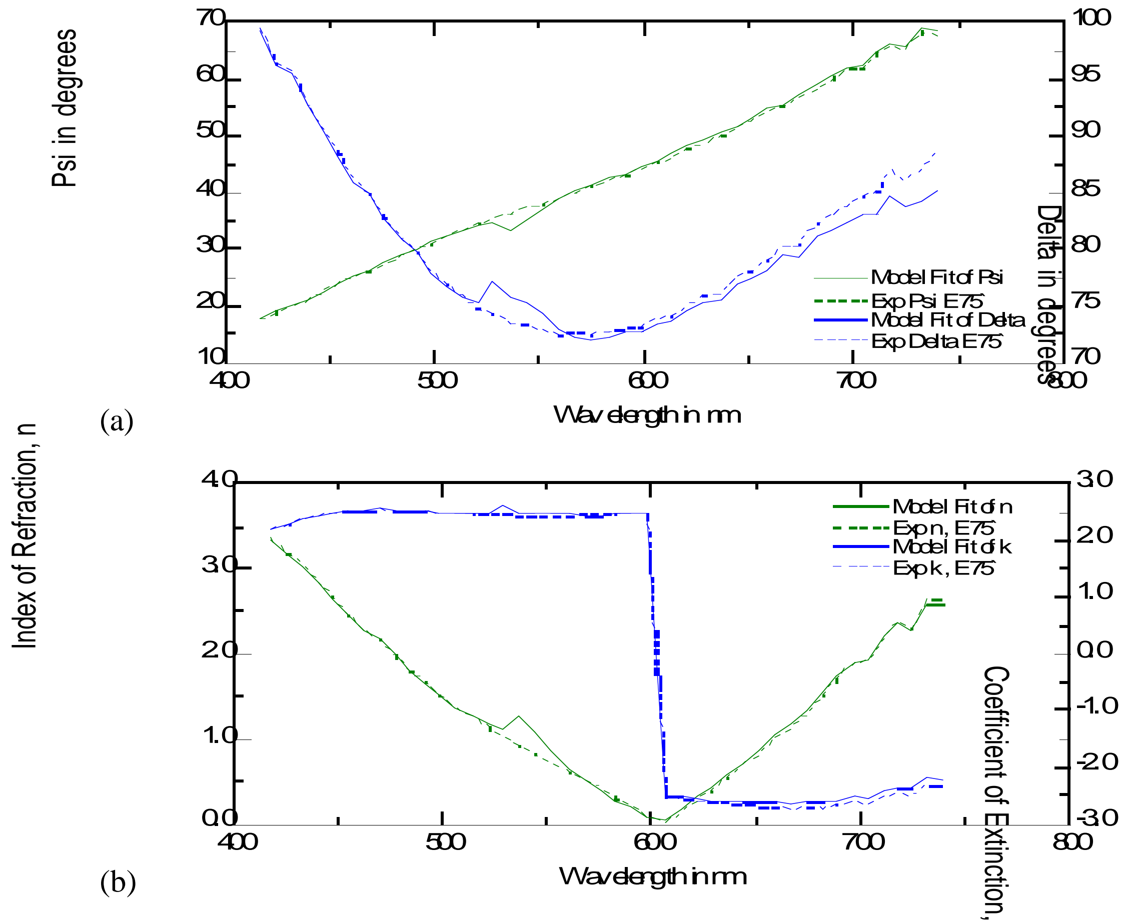

Figure 5. 8: Modified Slide B, experimental data and model fit data in terms of the wavelength of the incident polarized light. The model fit data derives from the model presented in figure 5.7. (a) Raw data directly from the ellipsometer, in terms of Psi and Delta. (b) Optical data, derived from the raw data using the Fresnel equations, in terms of the index of refraction, n, and the coefficient of extinction, k.

Unfortunately, not enough time was available to compare the optical fitted data of the individual modeled layers with standardized tables of optical properties, in order to determine the composition of the layers. In general, however, the decrease of the index of refraction with increasing wavelength suggests that all the component materials are transparent in the bulk. This agrees well with the macroscopic observation that the exposed areas are more translucent than the unexposed area. In addition, the thicker layer of SiO_2 modeled in slide B

suggests that the drastic change in both n and k at 600 nm evidenced in figure 5.8b is due to the extra deposition. It is still uncertain why this is the case, but the drastic change in n and k is suggestive of an optical resonance at that wavelength. More will be said about the possible application of this interesting feature in section 6.2.

Figures 5.9(a)-(c) are depth profiles of the optical properties of the implanted region, generated using the models of figures 5.3, 5.5, and 5.7. While a depth profile of this nature offers little insight in to the composition of the material, it is a convenient was of illustrating how the optical properties of the implanted glass changes as a function of depth, as well as their relative thickness to each other.

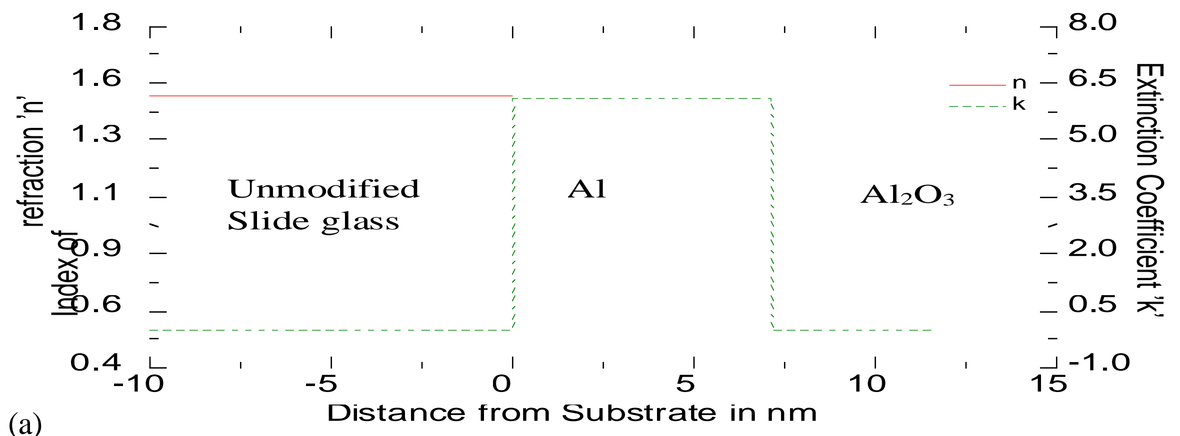

(a)

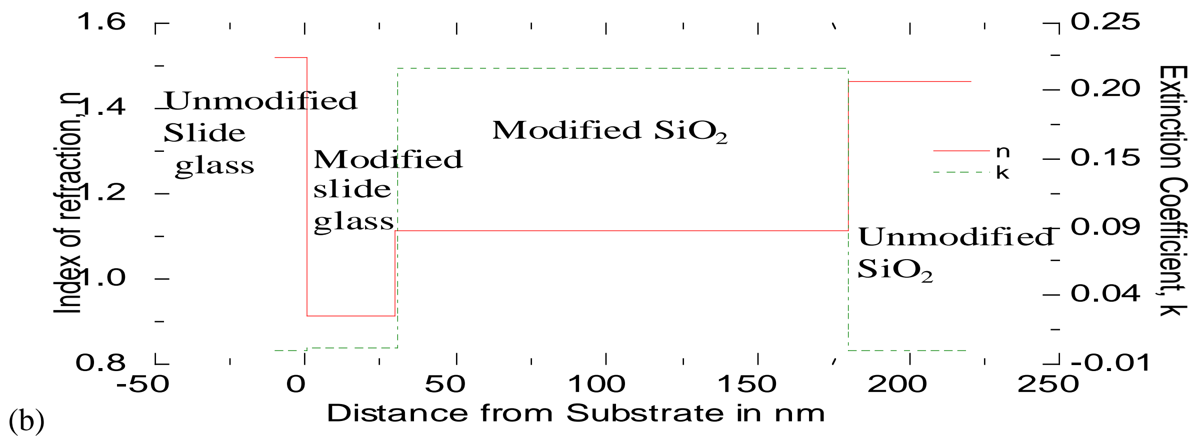

(b)

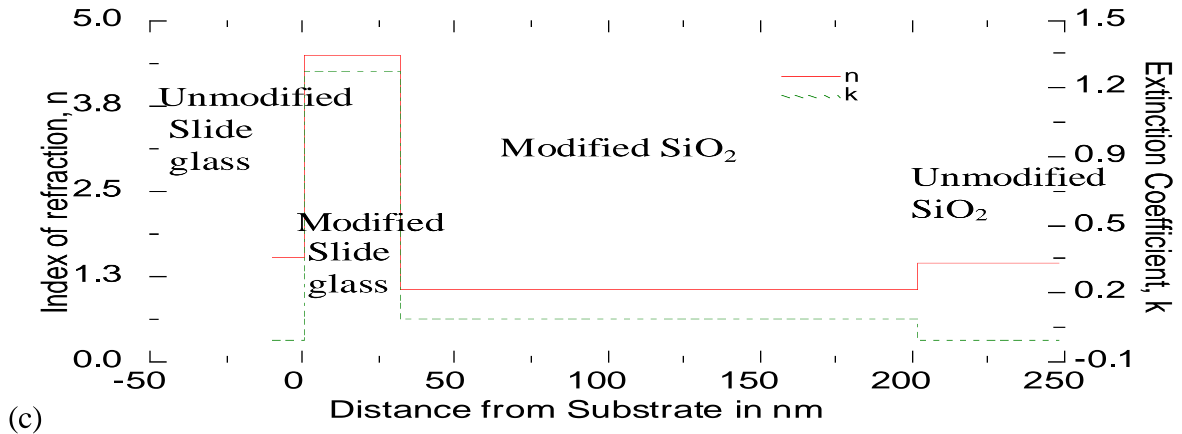

Figure 5. 9: Depth profiles of the optical constants for light of 500 nm as a function of depth from the unmodified region of the slide. Note how for each of the modified slides A and B, the first modified layer corresponds to an approximate depth predicted by Profile Code (30-40 nm), while the next two layers on top of it combine to total the 200 nm layer of SiO_2 deposited by sputtering. (a) Unmodified aluminum coated glass. (b) Modified slide A. (c) Modified slide B.

(a)

Layer	Material	n	k	Thickness
2	al2o3	n=0.60	k=0	4.3369 nm
1	al	n=0.60	k=6	7.1358 nm
0	slide	n=1.55	k=0	1 mm

(b)

Layer	Material	n	k	Thickness
3	sio2	n=1.45	k=0	39.999 nm
2	implanted sio2	n=1.15	k=0.20	150.08 nm
1	implanted slide	n=0.90	k=0.01	29.962 nm
0	slide	n=1.55	k=0	1 mm

(c)

Layer	Material	n	k	Thickness
3	sio2	n=1.45	k=0	46.393 nm
2	implanted sio2	n=1.0		169.86 nm
1	implanted slide	n=4.40		31.752 nm
0	slide	n=1.55	k=0	1 mm

Figure 5. 10: Summary table of the generated models, with n and k values for each respective layer. (a) Unmodified slide. (b) Slide A. (c) Slide B.

As can be seen by this summary of the models and constants arrived at, the geometry of the modified region is must be made very complex in order to fit the data. This complexity, with respect to the number and nature of the different films, suggests a highly complex modification process that is indicative of ion implantation into a continuously deposited layer of SiO_2.

n=0.60 k=0

5.4 Atomic Force Microscopy (AFM)

It was extremely difficult for me to examine the implanted area as a whole. This is because the maximum scanning area of the AFM is 50 μm by 30 μm. Instead, the AFM was used to look at the height drop across the transition from the unexposed region to the exposed region in the 100 μm masked hole. This not only provides confirmation at a very sensitive scale that even finely masked features can be modified, but it also gives information about how the deposition of SiO_2 depends on the aspect ratio of the mask.

A clear outline of part of the edge of the 100μm exposed region can be seen in the AFM graph of figure 5.11. In an ideal situation, where the SiO_2 deposition can be eliminated, the aluminum layer should be almost completely sputtered away from the exposed area, creating a height difference of approximately 9 nm between the exposed versus unexposed area. This is not the case, however; while the SiO_2 deposition is drastically reduced by the aspect ratio of the mask, it is not completely eliminated. As a result, the 9 nm drop is not observed here because it happens to be cancelled almost exactly by the SiO_2 deposition. This will be discussed later in this section. The raised outline of the exposed area can be explained

by accumulated SiO_2 on the walls of the mask which breaks off and remain on the surface of the glass. This too will be further discussed later in this section.

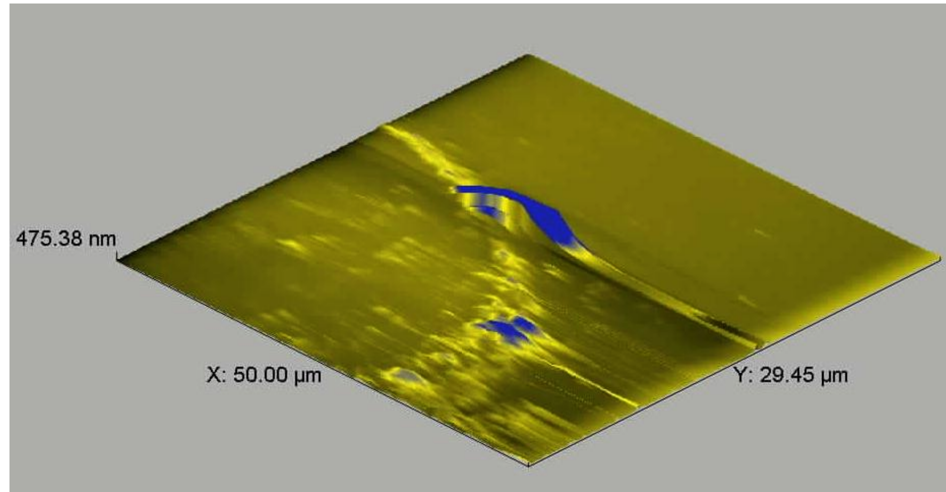

Figure 5. 11: AFM of the edge of the 100µm exposed area. The transition zone is the bumpy ridge outlining the partial circumference of a circle. The color is a false color supplied by the computer, and the z-axis is magnified by a factor of 100.

The image in figure 5.11 looks round, even though a round zone would normally not appear so, due to the aspect ratios of the AFM (50µm x 30µm). The relationship between the displayed result and the scanned area is shown the following figure:

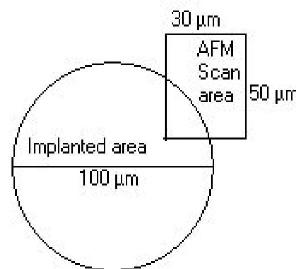

Figure 5. 12: Diagram of AFM scanning area relative to implanted area.

Cross-sections were also constructed of the AFM examined areas. Below is the same region as in Figure 5.11.

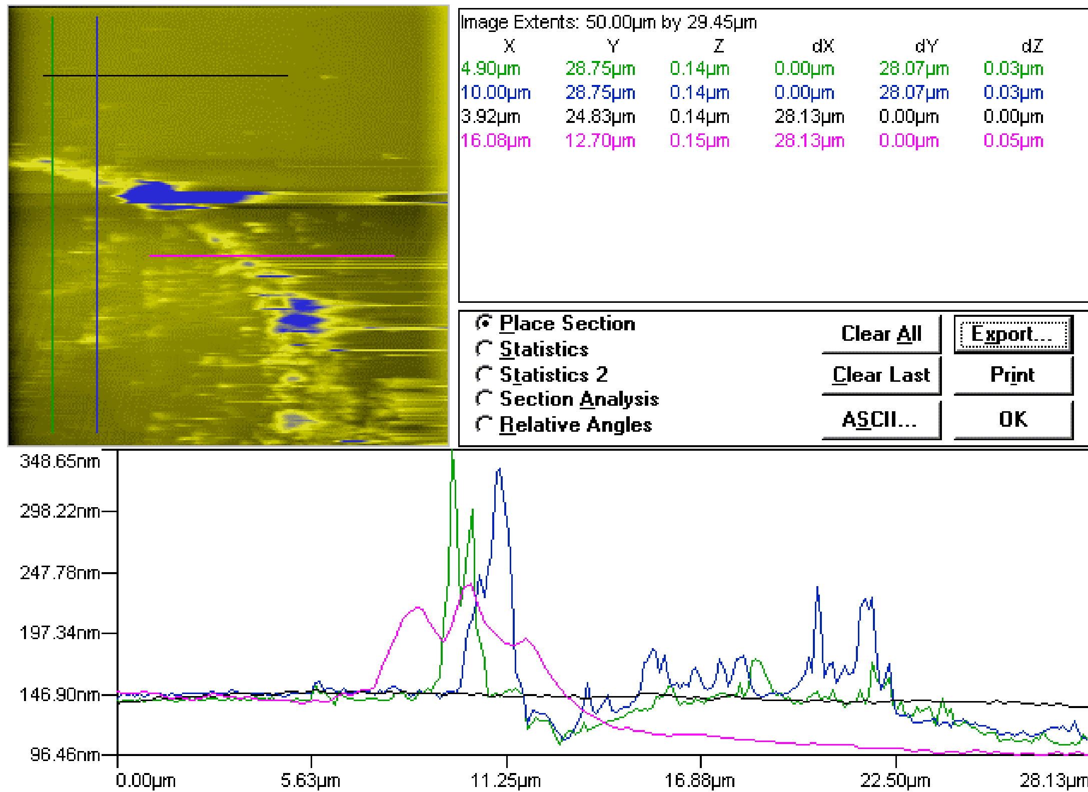

Figure 5. 13: Cross-section of figure 5.11. Each color graph of height vs. distance corresponds to a color used in the over-head view. Note how in every instance the height of the exposed area is approximately that of the unexposed area. Note as well how the transition region around the exposed area is at lest 50 nm higher than either of the other two areas.

There are a number of important features of the cross-section that need to be examined. As mentioned in the beginning of this section, the 200 nm deposition of SiO_2 is negligible in the exposed area due to the high aspect ratio of the mask opening to the mask depth. Deposition of the SiO_2 into trenches and other features is proportional to:

$$\Gamma_{SiO_2} \cup (1 - \cos(\theta_s))$$

Where θ_s is the angle subtended by the trench opening [25]. See figure 5.14a.

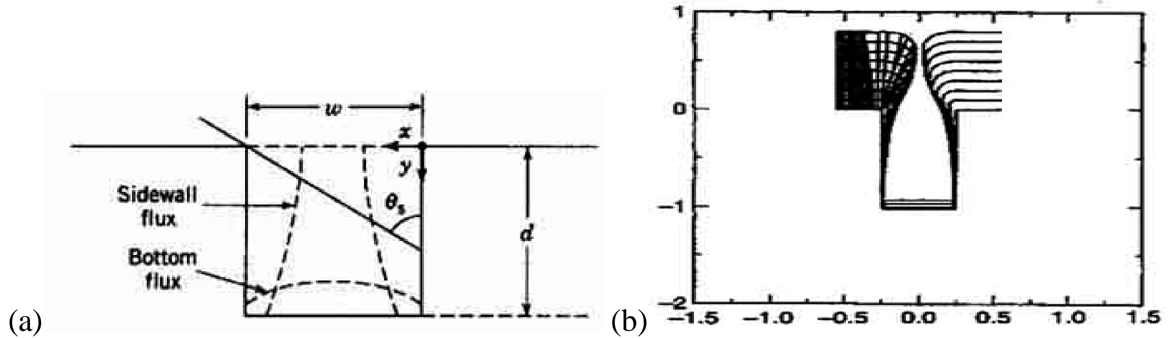

Figure 5. 14: Examples of deposition into trenches. (a) The dashed lines show the deposition on the walls and floor. Note the angle θ_s [25]. (b) SIMBAD model of a feature with a aspect ratio of 2.0 deposited almost to the point of aperture closure [28]. While the SiO_2 deposition discussed here is not this large an effect, the example is included to demonstrate how little material would arrive on the bottom of the trench under even the most extreme of circumstances.

For the 100μm in diameter hole, the depth of the mask is 200 μm, translating to an aspect ration of 2.0. The accumulation on the bottom would be the greatest in the center of the hole, where θ_s is:

$$\theta_s = (90 - \arctan\left(200/50\right) = 14.03^\circ$$

On the floor of the trench deposited material can impinge from both the left and the right, thus Γ is multiplied by an extra factor of two. Therefore for Γ, we get:

$$\Gamma_{bottom} \cong 2 \times \left(1 - \cos\left(14.03^\circ\right)\right) = 0.059$$

Since the deposition in areas that were not masked was approximately 200 nm, we can conclude that the most amount of SiO_2 on the bottom of the hole is

$$\Gamma_{bottom} = 200 \times 0.059 = 11.9 \text{ nm}.$$

In summation, the aspect ratio of 2.0 is the reason that the SiO_2 is not noticeable at the bottom of the AFM examined holes. Not only is the effect small, it actually cancels the similarly sized 9 nm indentation made by the sputtered away aluminum. As a result, the height of the exposed area is within a few nanometers to the unexposed area.

To explain why the transition area between exposed and unexposed region is so high, consider that SiO_2 accumulates on the vertical inside walls of the mask (see figure 5.14b). The SiO_2 on the wall connects with SiO_2 deposited on the surface of the slide. As a result, when the mask is removed, the accumulated SiO_2 does not necessarily break off cleanly. In some places it will instead break off the wall of the mask, resulting in the Òmountain-likeÓ formations surrounding the exposed area evident in figures 5.11 and 5.13. Noting two other features about the transition area evidenced in figure 5.13 further corroborates this conclusion. The height of the transition area (~200 nm at its highest point) relative to the depth of the mask (200 μm). This results in a ratio of 1000:1, suggesting that only a very small amount of the SiO_2 available in the mask to break away actually does. In addition, when comparing the width of the raised areas (~1 μm) to their height (200 nm), it is evident that these features are not spikes jutting off of the surface, but instead slight inclines which have been exaggerated by the z-dimension magnification factor of 100 used to make them more visible.

5.5 Secondary Electron Microscopy (SEM)

It is difficult to perform SEM on an insulating material. The same charging effects that hinder implantation into insulators reappears in the SEM. In this instance, however, the

aluminum coat that remains over the unimplanted areas after implantation proves to be of great use. For a short while, it continues to prevent charging, even in the implanted areas, where there is no coat. In addition, the aluminum coat is so thin that the secondary electrons pass through it unhindered. Thus, the morphology of both the implanted and unimplanted glass can be examined with ease.

The morphology of the areas that have been implanted bear a striking resemblance to similarly implanted glass, created by Battaglin [20], using beam ion implantation. Regardless of the optical model used, the fact that the SEM micrographs look very similar is strong evidence implantation of some sort has been achieved.

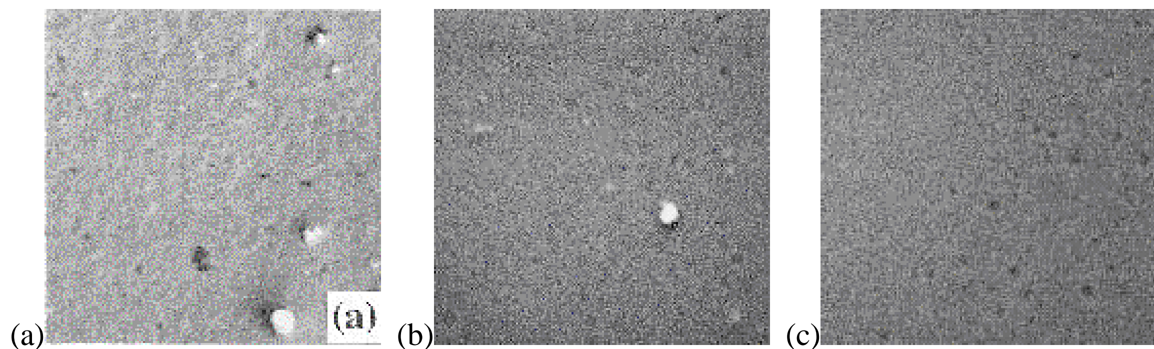

Figure 5. 15: SEM images of three implanted areas. (a) An implantation of argon into soda-lime glass, at a fluency of $7x10^{16}$ ions/cm^2 with ion energy of 125 keV [20]. (b) An implanted area of carbon dioxide made at 25 keV, to a dose of $6x10^{16}$ ions/cm^2. (c) Another implanted area of carbon dioxide made at 25 keV, to a dose of $6x10^{16}$ ions/cm^2. Note the similarities in the morphology of (a) to (b) and (c). Each picture measures 10μm on a side.

Although the energy is far greater, and argon was used instead of carbon dioxide, the energy density is approximately equal to what was achieved using PIII. This can be seen by comparing the profile code of the argon implantation (figure 5.16) with the carbon dioxide profile code (figure 4.4).

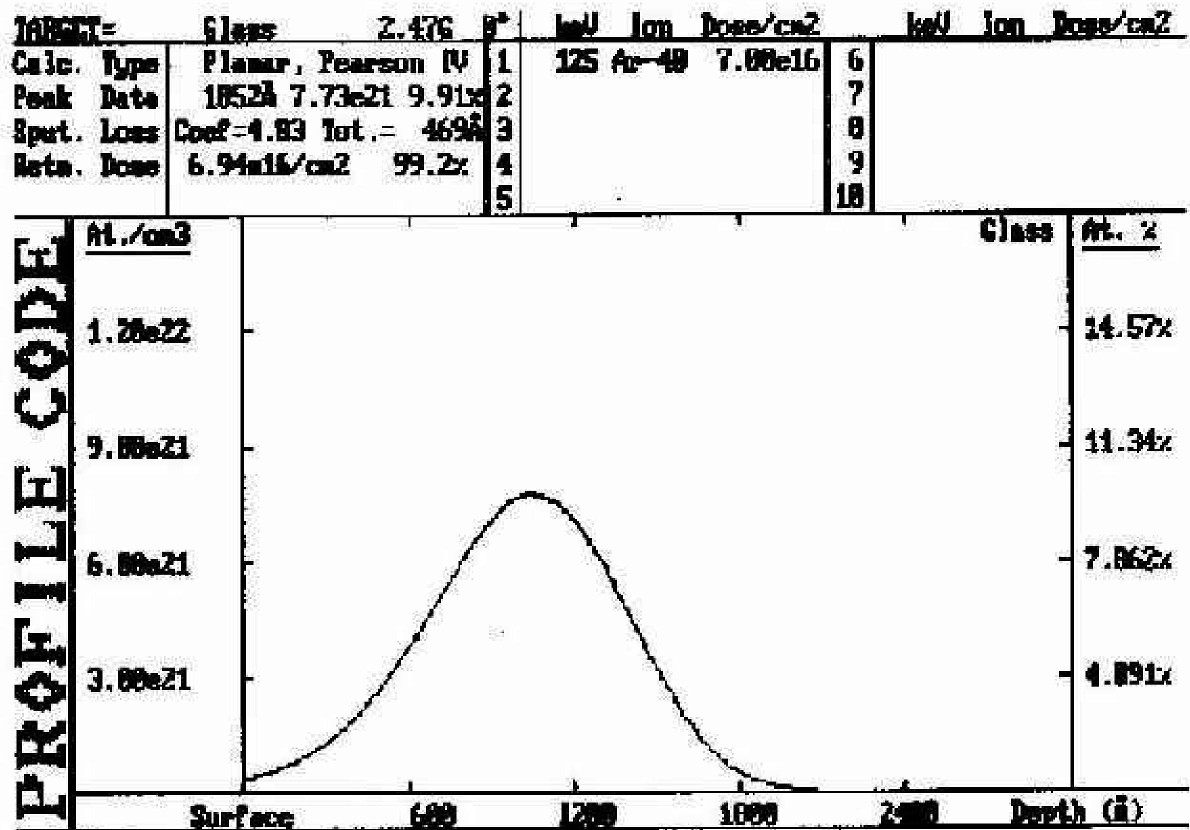

Figure 5. 16: Profile code of the implant of argon into glass, at fluency of $7x10^{16}$ ions/cm^2 with energies of 125keV.

The density of implanted argon ions at the surface of the argon-implanted sample is approximately $0.5x10^{21}$ ions/cm^3. This is approximately 1/16 the density at the surface of the carbon dioxide implant, $8x10^{21}$ ions/cm^3. The total energy density at the surface is almost identical, which is what accounts for the similarity of the SEM images. Thus, even though the fluence of ions is different, the amount of energy at the top layer is very similar, to within 8%.

Multiplying the total number of ions at the surface, $n_{surface}$, by the energy of each incident ion, E_{ion}, will arrive at the surface energy density.

$$\varepsilon_{argon} = n_{surface} \times E_{ion}$$

Thus, for the argon,

$$\varepsilon_{argon} = \left(0.5\times10^{21}\right)\times\left(1.25\times10^{5}\right) = 6.25\times10^{25}$$

For carbon dioxide, the ions must be broken into their component parts, due to the differing incident energy of oxygen versus carbon.

$$\varepsilon_{co_2} = \left[\left(2\times10^{21}\right)\times\left(7\times10^{3}\right)\right] + \left[\left(6\times10^{21}\right)\times\left(9\times10^{3}\right)\right] = 6.8\times10^{25}$$

The similarities in energy density is suggestive that implantation has occurred. In addition, however, the effects of implantation become clear when the morphology of an implanted region is compared with an unimplanted (figure 5.17). Note the lack of surface features that are present in the implanted images.

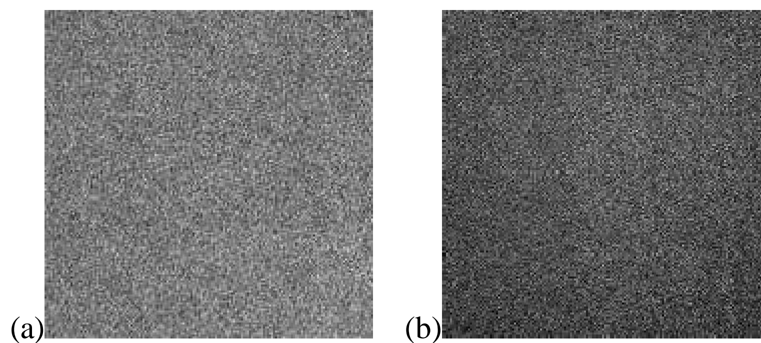

Figure 5. 17: SEM images of unimplanted areas. Note the contrast in morphology between these and the SEM images presented in figure 5.15. Each picture measures 10µm on a side.

The undamaged morphology or the unimplanted areas, in contrast with the damaged morphology of the implanted region, in combination with the implanted region's similarity in appearance and surface energy density to the argon beam implanted glass sample, is suggestive that "implanted glass" is continuously being deposited.

Chapter 6

Conclusion

6.1 Summary

The primary goal of this project was the to use PIII to modify the optical and electrical properties of an insulating material. This has been successful, and the modification of optical properties warrants further investigation. While modification has been demonstrated and the optical properties have been changed, the late discovery of a co-deposition during implantation has serious consequences for the future use of our apparatus for this purpose. Efforts to control which regime is employed, depositing or non-depositing, will be required. For cases were Si-based optical materials are being studied, the co-deposition may be useful and efforts to enhance it could be tried. These might include small quantities of gas additives (like CF_4) designed to add a chemical component to the physical removal, low pressure, low power, or an added bias source. Thus, although from the standpoint of our expected results for this thesis, this behavior was initially surprising, in the long run it points the way for an even wider range of utility for the William and Mary apparatus.

6.2 **Applications of this research**

Possible applications for plasma modified insulators is extremely broad; industrial applications of the specific findings of this research include:

<u>Optical wave-guides/ optical delay lines:</u> By SnellÕs law, total internal reflection can be achieved at angles greater than θ_c, where $\sin(\theta_c)=n_2/n_1$, n, being the index of refraction.

Thus, the dramatic shift in the index of refraction at approximately 600 nm (figure 5.8) suggests that total internal reflection of light is possible within two regimes. For low wavelengths, the implanted layer could serve as the wave-path, contrasting the high n of the implanted material with the relatively low n of the surrounding glass. For wavelengths slightly above 600nm, the glass could serve as the wave-path, reflecting off of the very low index of refraction of the implanted layer at that wavelength. If reliable total internal reflection is achieved, an optical wave-guide could be made, much like a fiber optic cable. It would be more flexible in design than standard fiber optical cable because it could have the planar geometries, in addition to those of a single line of light.

Similarly, with the high resolution attained by mask, to at least 50μm, swirling a thin line of implanted material out from the center of a pane of glass to the edge could create an optical delay line. If done correctly, a small pane of glass could add hundreds of meters of extra distance to the path a beam of light follows. An ideal application would be in compact optical switches, where space is at a premium.

A third feature of the wave-guide application is as a frequency selector. By changing the angle of incidence of incoming light the wavelength relative to the implanted layer could be changed drastically. Light of any frequency could be sent into the implanted zone. If angled correctly, the sudden drop in the index of refraction could disperse certain wavelengths by not preventing them from internally reflecting back into the wave path. Again, this is the sort of multifunction, compact, solid-state device that might be useful in miniature optical switches.

Security/ID cards: The high resolution attainable by this technique comes in useful for purposes of personal identification in high security situations. At 50µm, a personÕs fingerprint could easily be implanted into a piece of glass or clear plastic. The fingerprint could be quickly ÒreadÓ by a transmission beam of light diffracted through the fingerprint. Each personÕs diffraction pattern would be unique, but more importantly, each card would be unique. While the outline on a 50µm scale would be legible, the actual damage caused by the implant would be random. Hence, the glass or plastic fingerprint would be very difficult to replicate. The problem would be made even more difficult since the fingerprint is actually under the surface of the material, and as such protected from surface analysis.

Different implantation substrates: Other interesting applications would be to change the substrate insulator. Possibilities include other types of glasses, polymers, fiberglass, ceramics, organic materials, rubber, and crystals such as mica, quartz, sapphire or diamond. These are all materials for which the industrial effectiveness of implantation has largely been ignored because of the difficulty associated with beam implantation methods. With the ability to perform PIII insulators, that barrier has been removed, and a whole range of possibilities has opened.

6.3 Future Research

These are a few potential uses for this technology. More uses will be arrived at with further research. To this end, possible future goals of this project include:

Selection and Control of Modes of Operation: As mentioned in the conclusion, the William and Mary system will have to be modified in order to enable researchers to choose

between plasma generation via inductive coupling or via capacitive coupling. Possible modifications may include operating at higher power, the use of strong external magnetic fields, Faraday shielding, or the substitution or addition of other plasma sources to reduce window sputtering.

Modeling: Two modeling programs could be used to greatly aid this research. The first, TRIM code, could be used to track accurately the electric fields of the slide holder, to observe any effects they have on the implantation. The second, more important modeling would employ the SIMBAD program to help predict the deposition of SiO_2 as a function of aperture aspect ratio. Better understanding would aid in turning the SiO_2 deposition from an unexpected effect into a useful tool.

Obtaining a depth profile: An implantation using nitrogen would be of the most immediate benefit, even though it has little or no expected effect on the optical properties of glass. This is because nitrogen is easy to depth profile using XPS or SIMS, providing definitive evidence that implantation has occurred.

Exposing with different plasma species: Hydrogen, oxygen, carbon monoxide, methane, helium, nitrogen, and argon are all possible future species to implant. Carbon monoxide and methane would be interesting because of the possibility of growing a diamond-like film under the surface of the glass. In addition, helium, and argon are noble gases, and thus little has been published about their effects in glass.

A thicker aluminum coat: Currently, the limiting factor of both the deposited dose and the implantation depth is the thickness of the conductive coat. 100 is simply too thin and fragile to withstand more stressful implantation. A 200-500 coat of aluminum would

reduce the effect of losing the upper most atomic layers to oxidation, withstand sputtering due to implantation for longer, and support higher pulse voltages. While some incident ions would halt in the aluminum, rather than implant into the glass, the additional aluminum would not be enough to significantly impede implantation.

Chapter 7

Acknowledgements:

I would like to thank the following people: Dr. Manos, my advisor, for his guidance and wisdom in developing the ideas of and in writing this thesis. Lingling Wu for her patience and instruction in the uses of the implantation equipment. Dr. Hamann, of Siemens company, for cutting the micron holes used in the masks. Richard Proper for his willingness to help out with repairs and whatever else needed to be done. Carol Kalil for teaching me to use the SEM and the AFM. Amy Wilkerson for her company in the surface analysis lab. John Bensel, for his help with the design and construction of the slide holder. And finally Gina King, for her encouragement and support throughout this project.

References

[1] M.A. Lieberman, A.J. Lichtenberg. *Principles of plasma discharges and materials processing*. John Wiley & Sons, Inc., New York, 1st edition, 1994.

[2] Shu Qin, Chung Chan. *J. Vac. Sci Technol B.*, **12**(2) 962 (1994)

[3] M Tuszewski, J. T. Scheuer, I. H. Campbell, and B. K. Laurich. *J. Vac. Sci Technol B.*, **12**(2), 973 (1994)

[4] O. Demokan, E. Marji. *J. Appl. Phys.,* **85**(4), 2081 (1999)

[5] Shamin M. Malik, K. Sridharan, R. P. Fetherston, A. Chen, and and J. R. Conrad. *J. Vac. Sci. Technol.,* B **12**(2), 843 (1994)

[6] Jesse Matossian. *J. Vac. Sci Technol B.,* **12**(2), 850, (1994)

[7] Xiubo Tian, Xiaofeng Wang, Baoyin Tang, Paul K. Chu, Ping K. Ko, Yiu-Chung Cheng. *Rev. Sci. Instrum,.* **70**(3), 1824 (1999)

[8] A. G. Lui. *J. Appl. Phys.,* **84**(4), 1859 (1998)

[9] Z. M. Zeng, T. K. Kwok, X. B. Tian, B. Y. Tang, and P. K. Chu. *J. Appl. Phys.,* **86**(1), 120 (1999)

[10] Shamim M Malik, D. E. Muller, K. Sridharan, R. P. Fetherston, Ngoc Tran, and J. R. Conrad. *J. Appl. Phys.,* **77**(3), 1015 (1995)

[11] C. B. Franklyn, G. Nothnagel. *J. Vac. Sci Technol B.,* **12**(2), 923 (1994)

[12] J Chen. *J. Mat. Eng. Performance.,* **2**(6), 839 (1993)

[13] Shu Qin. *IEEE Trans. Plasm. Sci.,* **27**(3), 766 (1999)

[14] Lisa De Jong. *Plasma Source Ion Implantation for Improved Surface Hardness of Stainless Steel.* Honors Physics Thesis, College of William and Mary (1997).

[15] Anthony Richardella. *Plasma Source Ion Implantation Modeling Project*. Honors Physics Thesis, College of William and Mary (1999).

[16] M.M. Shamim, J. T. Scheuer, R. P. Fetherston, and J. R. Conrad. *J. Appl. Phys.,* **70**(9), 4756 (1991).

[17] Ling Ling Wu, D.M. Manos. ÒPattern Writing by Implantation in a Large-scale PSII System with Planar Inductively Coupled Plasma Source.ÓUnpublished paper, Dept. of Applied Science, College of William and Mary, 1999.

[18] Thomas J Venhaus. ÒPlasma Source Implantation of High Voltage Electrodes.ÓPhD dissertation presented to Dept of Applied Science, College of William and Mary, 1998.

[19] M. L. Johnson, D. M. Manos, T. Provost. *J. Vac. Sci Technol A.,* **15**(3), 763 (1997)

[20] G. Battaglin, G. W. Arnold, G. Mattei, P. Mazzoldi, J.C. Dran. *J. Appl. Phys.,* **85**(12), 8040 (1999)

[21] J. L. Buckner, D. J. Vitkavage, and E. A. Irene. *J. Appl. Phys.,* **63**(11), 5288 (1988).

[22] S. C. Vitkavage and E. A. Irene. *J. Appl. Phys.,* **64**(4), 1983 (1988)

[24] Levi, Leo. *Applied Optics*. John Wiley & Sons, Inc., New York, 1980.

[25] M. Ohring. *The Materials Science of Thin Films*. Academic Press, New York, 1st edition, 1992.

[26] J.E. Shelby. *Handbook of Gas Diffusion in Solids and Melts*. ASM International, Materials Park, OH, 1st edition, 1996.

[27] H.G. Tompkins, W.A. McGahan. *Spectroscopic Ellipsometry and Reflectometry*. John Wiley & Sons, Inc., New York, 1st edition, 1999.

[28] Ronald A Powell, Stephen Rossnagel. (Ed.) ÒPVD for Microelectronics: Sputter Deposition Applied to semiconductor Manufacturing.ÓThin Films Vol 26. Academic Press, New York. 1999